The Universality of inter-ELM Pedestal Fluctuations in AUG and DIII-D
Impacting the Edge Profile Structure by Clamping of the Gradients

F. M. Laggner, E. Kolemen
Princeton University
Princeton, United States of America
Email: flaggner@princeton.edu

A. Diallo, B. A. Grierson
Princeton Plasma Physics Laboratory
Princeton, United States of America

R. J. Groebner, T. H. Osborne, P. B. Snyder, the DIII-D Team
General Atomics
San Diego, United States of America

E. Wolfrum, M. Cavedon, F. Mink, the ASDEX Upgrade Team
Max Planck Institute for Plasma Physics
Garching, Germany

K. Barada
University of California Los Angeles
Los Angeles, United States of America

G. F. Harrer
Institute of Applied Physics, TU Wien, Fusion@ÖAW
Vienna, Austria

Abstract

For a wide range of operational parameters and in machines with different wall materials, namely ASDEX Upgrade (AUG) and DIII-D, the inter-ELM pedestal profile evolution has been robustly linked to characteristic fluctuations. These results indicate that similar instabilities might dominate the pedestal structure and its dynamics in between edge localized modes (ELMs). Furthermore, the comprehension of the underlying instabilities that determine the pedestal structure is advanced because the electron density as well as temperature gradients were found to become clamped in distinct phases of the ELM cycle. The general behavior of the inter-ELM fluctuations supports that similar mechanisms will determine the pedestal of future fusion devices. This stresses the necessity that predictive models need to incorporate a robust mechanism, which describes the clamping of individual profile gradients across wide ranges of pedestal parameters. The inter-ELM fluctuations exhibit a similar sequence of their onsets in AUG and DIII-D. This gives strong evidence that their origin is the same, although both machines usually operate in different parameter regimes. Generally, low fluctuation amplitudes are found during the initial recovery of the maximum electron density gradient. After this phase, the maximum electron density gradient saturates and simultaneously medium frequency, pedestal localized fluctuations set in. The electron temperature pedestal evolves further and the saturation of the maximum electron temperature gradient correlates with the onset of high frequency fluctuations. Fast vertical plasma oscillations were utilized as a tool to probe the pedestal fluctuations as well as the pedestal stability. Such oscillations perturb the edge current. To make them an effective ELM pacing method, the pedestal must evolve close to its gradient saturation. This state is stable, but marginal to the stability limit. When the pedestal is perturbed, e.g. by a modification of the edge current, it is highly probable that an ELM crash is triggered.

1. Introduction and motivation

The high confinement mode (H-mode) [1, 2] is the designated operation scenario for ITER [3], because of its improved plasma confinement. Its origin lies in the establishment of an edge transport barrier (ETB), which leads to a steep pressure gradient at the plasma edge, commonly referred to as pedestal. The pedestal pressure is globally limited by edge localized modes (ELMs) [4, 5], which periodically relax the ETB.

The governing model for instabilities underlying the ELM-related pedestal limit is the destabilization of coupled peeling-ballooning (PB) modes [6]. These exhibit critical growth above certain edge pressure gradients and edge

current densities. To predict the pedestal height, i.e. the pressure increase at the plasma edge, which is directly related to the global plasma performance, another constraint is required. Here, the EPED model assumes the onset of kinetic ballooning modes (KBMs), which limit the pressure gradient evolution at sub-critical level, i.e. below the PB stability limit [7, 8]. Since microinstabilities like KBMs can contribute to additional particle and heat fluxes across the pedestal, without leading to a global instability like an ELM crash, they are a good candidate to affect the inter-ELM profile evolution. Detailed modelling performed on pedestals of a variety of machines find several microinstabilities being present [9, 10, 11, 12, 13, 14, 15].

Experimentally, instabilities, which express themselves as fluctuations of diagnosable quantities, i.e. magnetic field fluctuations, density fluctuations, temperature fluctuations or a combination of them, have been identified to appear in distinct phases of the ELM cycle [16, 17, 18, 19]. Further, their onset is linked to the inter-ELM evolution of the pedestal profiles. The correlation of the profile evolution and the fluctuation onset indicates that these might be causally linked and the underlying instability could play a dominant role in determining the pedestal structure.

The aim of this work is to compare the characteristics of the observed inter-ELM fluctuations as well as the pedestal profile evolution between ASDEX Upgrade (AUG) and DIII-D. It is found that the electron (and ion) density as well as temperature gradients become clamped in different phases of the ELM cycle [20]. These distinct phases are further accompanied by characteristic fluctuations, indicating that several instabilities located at distinct radial positions in the pedestal set in. These findings challenge predictive pedestal models and motivate the incorporation of instabilities that are present over wide ranges of experimental parameters as covered by AUG and DIII-D.

2. MACHINE COMPARISON OF AUG AND DIII-D

AUG and DIII-D are well diagnosed [21, 22], medium sized tokamaks with similar aspect ratio. The lower divertor of AUG is optimized for plasma exhaust and neutral compression. Another difference is that AUG is slightly smaller than DIII-D, which is also reflected in a smaller plasma volume. DIII-D has unique capabilities for plasma shaping because of its 18 shaping coils inside the toroidal field coils [23]. The major difference between both experiments is the material of the first wall. AUG has all of its plasma facing components (PFCs) covered with tungsten (W) [24], which is a reactor relevant first wall material choice but it imposes operational boundaries [25]. DIII-D has carbon (C) PFCs [26] enabling low plasma collisionality (ν^*) operation without suffering from radiation associated with impurity contamination.

Figure 1 compares the poloidal cross sections of both machines, plotted for similar ranges of R and z, and indicates the various diagnostics that are utilized in this study and their location with respect to the plasma column. The compared plasmas are both lower single null (LSN) with the $\nabla B \times B$ drift direction to the lower X-point. While the lower divertor of AUG is closed, the lower divertor of DIII-D is open, i.e. the compared discharges likely have different divertor and scrape-off layer conditions. The presented discharge of AUG was performed at a toroidal magnetic field (B_ϕ) of 2.47 T and plasma current (I_p) 1 MA, whereas the DIII-D discharge was performed at B_ϕ 2.04 T and I_p 1.2 MA. This results in different edge safety factor (q_{95}): For the AUG discharge q_{95} is roughly 4.3 and for the DIII-D discharge it is 3.8.

Both discharges were externally heated: 4.7 MW of neutral beam heating power (P_{NBI}) and 1.1 MW of electron cyclotron resonance heating power (P_{ECRH}) (for central impurity control) were injected into the AUG plasma, whereas a P_{NBI} of 1.9 MW was put into the DIII-D plasma. Both discharges had a relatively low ELM repetition frequency (f_{ELM}) with long inter-ELM periods, enabling detailed profile analyses as discussed in sections 2.1 and 2.2. The f_{ELM} in the AUG discharge was 40 Hz and it was 15 Hz in the DIII-D discharge. Owing to the higher gas puff, required to operate with the W wall, the line averaged electron density (n_e) in the AUG discharge was $9.0 \cdot 10^{19}$ m^{-3}, while in the DIII-D discharge it was approximately $6.5 \cdot 10^{19}$ m^{-3} (roughly 25 % lower).

2.1. Utilized Plasma Diagnostics and Performed Analyses of AUG data

This paper mainly focuses on the investigation of the evolution of the maximum electron density gradient (max($-\nabla n_e$)) and maximum electron temperature gradient (max($-\nabla T_e$)) in the pedestal region throughout the ELM cycle. On AUG, the corresponding profiles are evaluated with a temporal resolution of 250 μs using the integrated data analysis (IDA) approach [27], which combines data of multiple plasma diagnostics. For the presented n_e profiles, the laser interferometry (LI) diagnostic [28] (measuring in the core n_e) has been combined with the lithium beam (LIB) diagnostic [29] (measuring the edge n_e). The recently refurbished electron cyclotron emission (ECE) diagnostic [30] together with an electron cyclotron forward model [31] have been used for the reconstruction of
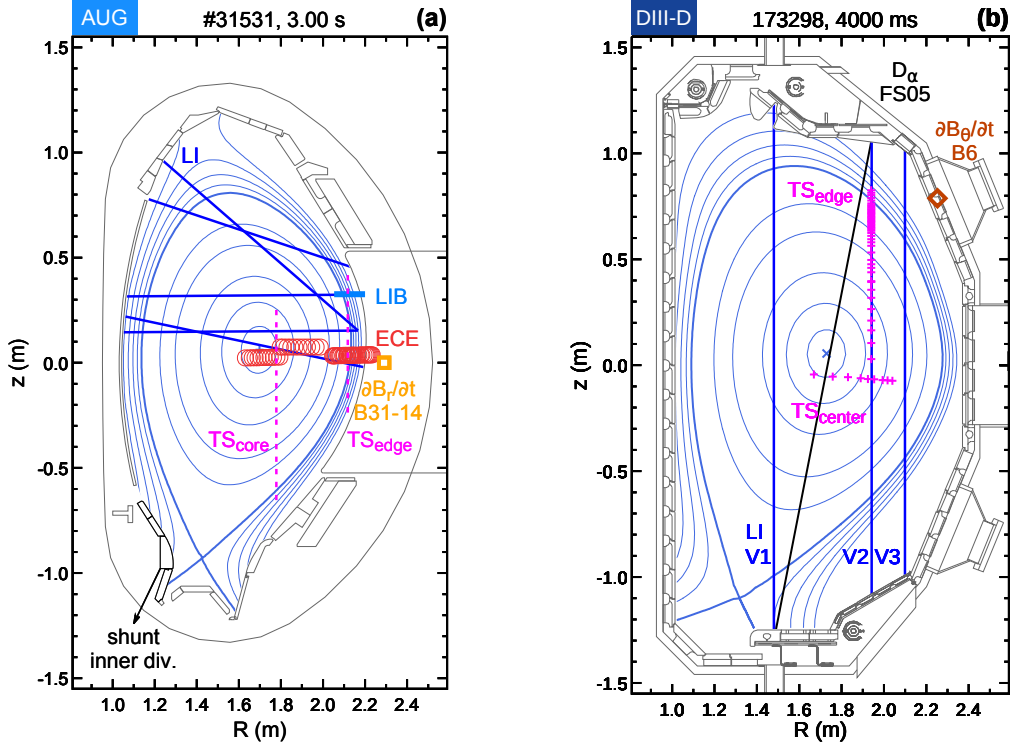
Figure 1: *Poloidal plasma cross sections and utilized plasma diagnostics: (a) AUG and (b) DIII-D. The ELMs are detected by shunt current measurements in the inner divertor of AUG (a, black) and by a filterscope measuring D_α line radiation (D_α) from the outer divertor of DIII-D (b, black). The pedestal profiles are measured by Thomson scattering (TS) (magenta), laser interferometry (LI) (blue), electron cyclotron emission (ECE) (red) and lithium beam (LIB) (light blue). Radial magnetic field fluctuations ($\partial B_r/\partial t$) (orange) and poloidal magnetic field fluctuation ($\partial B_\theta/\partial t$) (dark orange) are detected by Mirnov coils.*

electron temperature (T_e) profiles. Furthermore, the relative alignment of the n_e and T_e profiles is cross checked with the Thomson scattering (TS) diagnostic [32]. As ELM monitor a shunt current measurement from the inner divertor is used [33]. The locations of the utilized plasma diagnostics in the poloidal plane are also presented in figure 1 a.

2.2. Utilized Plasma Diagnostics and Performed Analyses of DIII-D data

The TS system at DIII-D is the main n_e and T_e profile diagnostic [34, 35]. There is an edge system with high spatial resolution available and multiple lasers allow for a high temporal resolution. The profile data has been fitted in time and spatial domain within the OMFIT framework [36] using the OMFITprofiles module [37], which has been extended to perform ELM synchronized analysis. Furthermore, for line integrated n_e fluctuation measurements, the high temporal resolution LI (sampling rate of 1.67 MHz) has been deployed [38, 39]. The ELMs are monitored by a D_α line radiation (D_α) filterscope looking into the lower outer divertor region [40, 41]. The locations of all introduced plasma diagnostics can be found in figure 1 b.

3. INTER-ELM PEDESTAL PROFILE EVOLUTION AND FLUCTUATION ONSET

In AUG and DIII-D several studies have been performed on the pedestal structure and its inter-ELM evolution of the pedestal profiles [42, 43, 44, 45, 21, 46] as well as on pedestal localized fluctuations [47, 48, 49, 50] and their connections [17, 51, 52]. In the following, the two plasma discharges, which were introduced in section 2, are compared with respect to their inter-ELM profile evolution and the onset of pedestal localized fluctuations. Figure 2 presents the ELM synchronized pedestal gradients and ELM synchronized spectrograms of magnetic fluctuations, which are detected by Mirnov coils (MCs) (see figure 1).

In both machines, the max($-\nabla n_e$) saturates after Δt_{n_e} (light gray vertical bar) and medium frequency fluctuations in the range of 100 kHz set in. The T_e pedestal evolves for an additional time Δt_{T_e} (gray vertical bar) and a saturation of the max($-\nabla T_e$) correlates with the onset of high frequency fluctuations (in the region of 300 kHz). During the last phase of the ELM cycle the maximum pressure gradient is clamped and the signature of the 300 kHz (high frequency) fluctuations is also detected on the high field side (HFS) [19]. Although
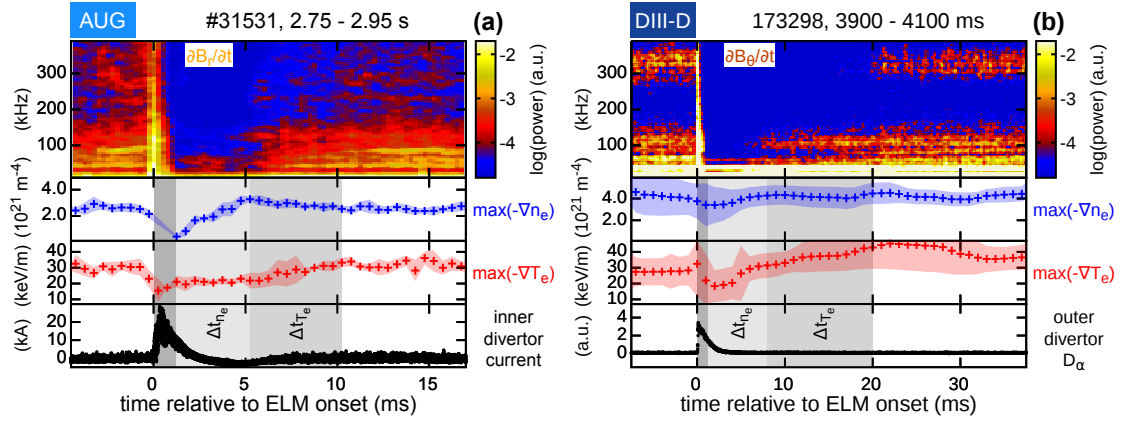
Figure 2: *Inter-ELM fluctuations and evolution of the maximum profile gradients: (a) AUG and (b) DIII-D. ELM synchronized frequency histograms of radial magnetic field fluctuations ($\partial B_r/\partial t$) or poloidal magnetic field fluctuation ($\partial B_\theta/\partial t$) (top), evolution of the maximum electron density gradient ($\max(-\nabla n_e)$) (blue), maximum electron temperature gradient ($\max(-\nabla T_e)$) (red) and ELM monitor (black). In both cases the $\max(-\nabla n_e)$ saturates after a time Δt_{n_e}, which is accompanied by the onset of fluctuations in the range of $100\,\text{kHz}$; $\max(-\nabla T_e)$ evolves an additional Δt_{T_e} before it saturates, which is accompanied by fluctuations appearing around $300\,\text{kHz}$.*

the length of the inter-ELM period is different for the two presented cases, a characteristic sequence of profile recovery phases as well as the linked onsets of the inter-ELM pedestal fluctuations is identified. This suggests that the underlying pedestal instabilities are associated to the pedestal profile evolution. Their signature can be observed as characteristic fluctuations, appearing in the distinct phases of the inter-ELM pedestal profile recovery.

To provide a more comprehensive picture of the pedestal dynamics and their implications, several variations were performed in AUG and DIII-D. In section 3.1, n_e fluctuations and the impact of ELMs on them are studied. Further, a variation of triangularity (δ) has been performed at AUG to investigate the structure of the pedestal localized fluctuations for varied plasma shapes (section 3.2).

3.1. n_e Fluctuations across the Plasma Cross Section in DIII-D

Figure 3 compares ELM synchronized spectrograms of n_e fluctuations from three different vertical chords of the LI system (see figure 1 b). On the most central chord (V1) a low frequency core mode and its harmonics are visible. Further outwards at chord V2, besides the low frequency core activity broadband fluctuations are visible (between $100\,\text{kHz}$ and $300\,\text{kHz}$). These approximately set in after half of the $\max(-\nabla n_e)$ pedestal recovery phase. This observation points out that the ELM induced flattening of the profiles and the corresponding loss of energy instantaneously reduces the drive for instabilities that are located inside of the pedestal region. Therefore, even fluctuations measured around mid-radius (chord V2 and V3) can be affected by ELM crashes and their re-establishment after ELMs requires their drive to recover first. At the outermost chord (V3) the broadband fluctuations are present too. Additionally, a low frequency band appears at the end of the $\max(-\nabla n_e)$ recovery and it chirps down to $50\,\text{kHz}$. Since its onset time is very similar to
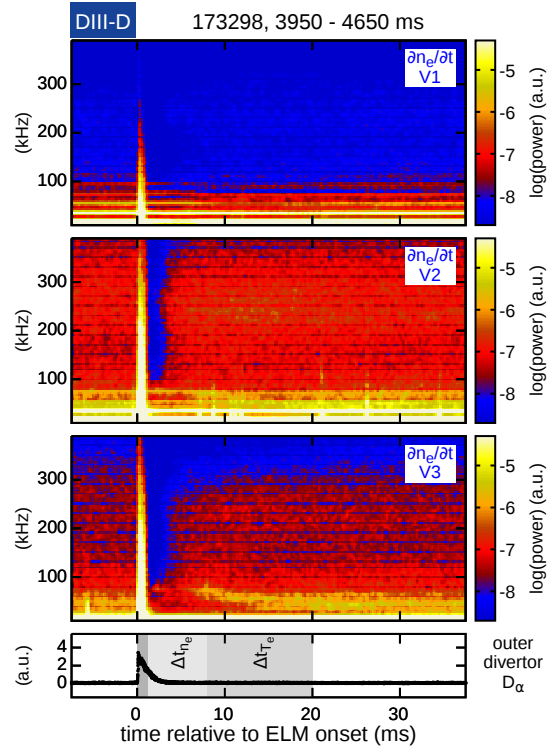

Figure 3: *ELM synchronized spectrograms of n_e fluctuations measured by laser interferometry (LI): From a central chord (V1) towards the edge (V3). While core mode activity dominates the spectrograms in the center, broadband fluctuations disappear immediately after the ELM crash due to vanishing drive. At the edge a low frequency fluctuation sets in after the initial recovery of the $\max(-\nabla n_e)$ and chirps down.*
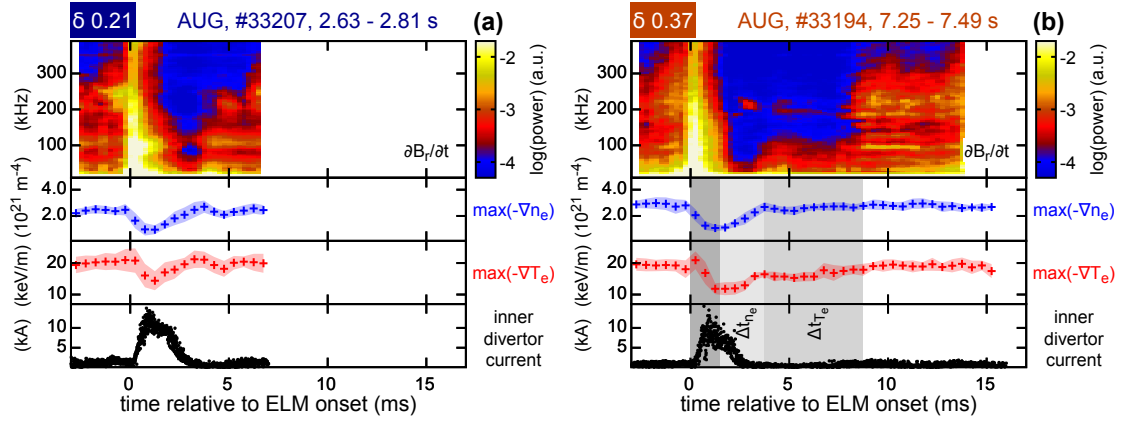
4

Figure 4: *Inter-ELM fluctuations and their relation to the pedestal evolution for varied plasma shaping: ELM synchronized frequency histograms of $\partial B_r/\partial t$ (top), evolution of the $\max(-\nabla n_e)$ (blue), $\max(-\nabla T_e)$ (red) and divertor shunt current (black) at (a) low δ and (b) high δ. Although, the duration of the inter-ELM period varies with δ, the sequence of the pedestal recovery phases and the associated onset of fluctuation bands remain the same.*

the 100 kHz fluctuations that are observed in the magnetics (see figure 2 b), the underlying instabilities might be somehow connected.

3.2. Pedestal Evolution and Inter-ELM Fluctuations at Varied Triangularity in AUG

Plasma shaping, e.g. δ, affects the edge stability and pedestal structure [53, 54] as well as the inter-ELM profile evolution [55]. For this reason, δ might also have impact on the inter-ELM pedestal fluctuations. Two discharges of AUG with varied upper δ are compared in figure 4. These were conducted with the same I_p, B_ϕ as well as similar gas puff and heating. As observed in the discharges presented in figure 2, a low amplitude of $\partial B_r/\partial t$ is observed over the whole spectral range during the initial recovery of the $\max(-\nabla n_e)$. After this phase, the $\max(-\nabla n_e)$ saturates and medium frequency fluctuations set in. In the case at lower δ, the f_{ELM} is significantly higher and inter-ELM period is only about 5 ms. Therefore, a distinction of the gradient recovery phases is rather challenging. In the case with higher δ, a further evolution of $\max(-\nabla T_e)$ can be identified (c.f. figure 4 b), which then saturates accompanied by the onset of the high frequency fluctuations.

The sequence of onsets of the fluctuations occur independently of δ, as demonstrated when comparing figures 4 a and 4 b. Even at low δ, the high frequency fluctuations at 250 kHz appear for a very brief period of roughly 2 ms. Since the sequence of the onsets of fluctuation bands remain the same, this gives strong evidence that the underlying instability causing the fluctuations is not sensitive to plasma shaping.

The duration of the inter-ELM period varies with δ. One possible explanation is outlined as follows: The extended PB boundary at higher δ allows for a higher pedestal. Assuming similar pedestal recovery rates for both cases, this would mean that it simply takes longer to get to a higher pedestal in the high δ case. Therefore, the pedestal profile recovery phases are extended. The extension of the pre-ELM phase with clamped pressure gradients at high δ might be more related to the pedestal localized fluctuations. These could clamp the pedestal in a PB stable configuration, i.e. regulate the pedestal profiles to be saturated away from the PB limit. Therefore, the following ELM crash becomes less likely than in the low δ case.

4. Probing the Inter-ELM Pedestal Fluctuations and Pedestal Stability by Vertical Oscillations

Vertical oscillations of the plasma column, often referred to as vertical kicks or jogs, have been widely used to pace ELMs [56, 57, 58, 59, 60], i.e. to increase the f_{ELM} above the natural one and therefore, reduce the size of the individual ELM crash. When the edge pressure gradient is saturated, the pedestal is stable but marginal to the PB stability limit. At DIII-D fast vertical oscillations, which apply a perturbation to the edge current density, were used as a tool to probe the pedestal stability as well as the robustness of the pedestal fluctuations.

In figure 5 it can be seen that immediately after a requested plasma down shift, an ELM crash is triggered. In comparison to the 'natural' ELM crashes, which appear in between the applied plasma oscillations, there is only a very brief period with saturated high frequency fluctuations (around 300 kHz) before these 'paced' ELMs. As
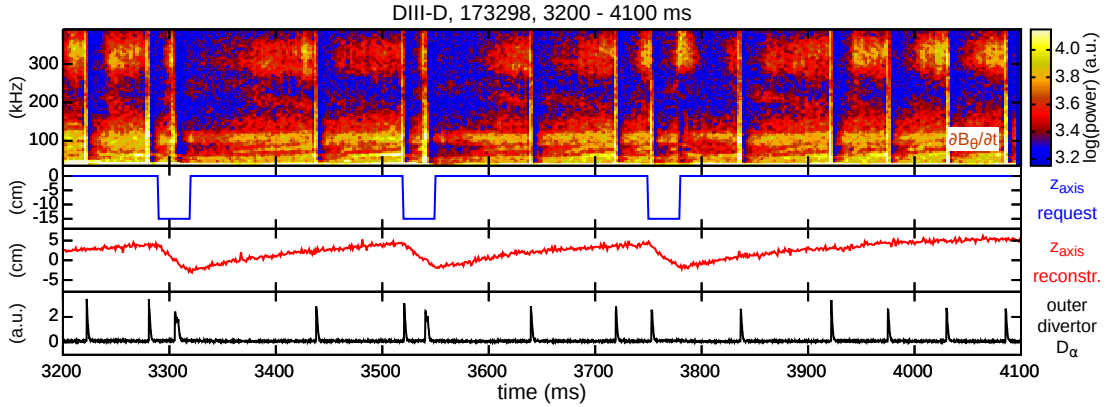
5

Figure 5: *Inter-ELM magnetic fluctuations and their interaction with vertical plasma oscillations: Spectrogram of $\partial B_\theta / \partial t$ (top), requested vertical position of the magnetic axis (blue), reconstructed vertical position of the magnetic axis (red) and a D_α measurement (black). When plasma oscillations are applied an ELM crash is triggered. Before this ELM crash, the inter-ELM fluctuations do not have a longer period of full saturation.*

discussed previously, each ELM crash leads to a collapse of the pedestal and its corresponding profile gradients and the pedestal localized fluctuations disappear. Then the pedestal profiles recover and corresponding to each profile recovery phase, the corresponding fluctuations set in. Interestingly, the 'paced' ELMs occur immediately after the high frequency fluctuations appear. This indicates that the pedestal builds up towards its pre-ELM saturated level before the 'paced' ELM crash is triggered. In other words this means that the applied perturbation can only trigger an ELM when the pedestal structure is close enough to its stability limit. Such kind of behavior becomes of importance when such vertical oscillations are used for ELM pacing.

To reliably trigger an ELM crash by an edge current perturbation, the pedestal must evolve up to a state where it is close to its stability limit. For this reason ELMs can not be paced at arbitrary f_{ELM}. A certain 'lag time' needs to pass in which the pedestal is re-established, as also observed when ELMs are paced with pellets [61]. This might raise concerns for the applicability of ELM pacing techniques in ITER, where the expected natural, f_{ELMs} is significantly smaller than the required one to protect the divertor from ELM energy losses [62]. If ELMs would need to be paced faster than the pedestal recovery time, the pacing efficiency might decrease significantly. Further, it was observed on DIII-D that the ELM induced parallel heat flux to the divertor is inversely related to the linearly most unstable mode number from PB analysis [63]. For this reason, vertical plasma oscillations, perturbing the the edge current, might actually tend to cause low mode number peeling modes, which would accordingly result in relatively larger ELM losses.

5. SUMMARY AND CONCLUSIONS

A comparison of the inter-ELM pedestal evolution and the associated pedestal localized fluctuations was performed between AUG and DIII-D discharges. Though both machines have different ranges of operational parameters and different PFCs materials, the inter-ELM evolution of the maximum pedestal gradients is shown to have a similar sequence of recovery phases. These phases were robustly linked to the onset of characteristic pedestal localized fluctuations, indicating that similar instabilities govern the pedestal structure and its dynamics in between ELMs. It was previously found that the underlying instabilities, causing the observed fluctuations, are localized in the pedestal region [17]. On AUG, further studies localized the fluctuations close to the minimum of the radial electric field ($\min(E_r)$) [19, 51] (high frequency band that appears with the $\max(-\nabla T_e)$ clamping) and further outwards close to the separatrix [48] (medium frequency band that appears with the $\max(-\nabla n_e)$ clamping). Besides the observation of similar inter-ELM behavior of the pedestal fluctuations in AUG and DIII-D, very similar observations were made in several other machines. In JET such kind of fluctuations were named 'washboard modes' [64]. The pedestal profile evolution was also linked to the fluctuations onset in Alcator C-Mod [16]. Furthermore, similar observations regarding inter-ELM pedestal localized fluctuations were made in EAST [65, 66], HL-2A [67] and PBX-M [68].

The combination of the presented results and similar observations reported from several machines supports that similar mechanisms might determine the pedestal structure in future fusion devices as ITER. Further, the conducted work underlines the necessity that predictive pedestal models have to incorporate a robust mechanism,

describing separate clamping of $\max(-\nabla n_e)$ and $\max(-\nabla T_e)$ over wide ranges of pedestal parameters. The corresponding instabilities must be independent of main ion species [69] and plasma shaping (c.f. section 3.2).

Generally, low fluctuation amplitudes are found during the initial recovery of the maximum electron density gradient. This is further observed in the plasma core, where broadband n_e fluctuations are strongly reduced during half of the initial recovery phase of the $\max(-\nabla n_e)$. Likely, their drive vanishes due to the energy loss caused by the ELM crash. Afterwards the drive needs to recover, leading to a period in which the whole plasma is relatively quiet.

In the last phase of the inter-ELM profile evolution the pedestal reaches a state of saturated gradients, which is marginal to the PB stability limit. If a perturbation, e.g. of the edge current, is applied to this state, as done with the vertical plasma oscillations, it becomes highly probable that an ELM crash is triggered. This implies that ELMs can not be paced at arbitrarily high frequency. It is a necessity that the pedestal builds up towards its stability limit such that the applied perturbation can become effective to trigger an ELM. The connection of ELM pacing probability and pedestal evolution becomes especially important in large scale devices as ITER, where the natural ELM energy losses exceed the material limit of the divertor. Here, a reduction of the individual ELM energy loss is required but it is also desired to achieve this without degradation of pedestal performance. The observation that the pedestal needs to build up towards its stability limit to enable efficient ELM pacing could also imply that the individual ELM loss, which is directly related to the pedestal pressure, cannot be reduced arbitrarily. Therefore, the relation between ELM energy loss reduction and ELM pacing efficiency has to be identified to ensure a safe operation of ITER with high pedestal performance.

DISCLAIMER

This report was prepared as an account of work sponsored by an agency of the United States Government. Neither the United States Government nor any agency thereof, nor any of their employees, makes any warranty, express or implied, or assumes any legal liability or responsibility for the accuracy, completeness, or usefulness of any information, apparatus, product, or process disclosed, or represents that its use would not infringe privately owned rights. Reference herein to any specific commercial product, process, or service by trade name, trademark, manufacturer, or otherwise does not necessarily constitute or imply its endorsement, recommendation, or favoring by the United States Government or any agency thereof. The views and opinions of authors expressed herein do not necessarily state or reflect those of the United States Government or any agency thereof.

REFERENCES

[1] A. E. Hubbard, Plasma Phys. Control. Fusion, **42**, A15 (2000)

[2] F. Wagner, Plasma Phys. Control. Fusion, **49**, B1 (2007)

[3] M. SHIMADA, D. J. CAMPBELL ET AL., Nucl. Fusion, **47**, S1 (2007)

[4] H. Zohm, Plasma Phys. Control. Fusion, **38**, 105 (1996)

[5] A. W. Leonard, Phys. Plasmas, **21**, 090501 (2014)

[6] P. B. SNYDER, H. R. WILSON ET AL., Phys. Plasmas, **9**, 2037 (2002)

[7] P. B. SNYDER, R. J. GROEBNER ET AL., Phys. Plasmas, **16**, 056118 (2009)

[8] P. B. SNYDER, R. J. GROEBNER ET AL., Nucl. Fusion, **51**, 103016 (2011)

[9] D. DICKINSON, C. M. ROACH ET AL., Phys. Rev. Lett., **108**, 135002 (2012)

[10] S. SAARELMA, M. N. A. BEURSKENS ET AL., Nucl. Fusion, **53** (2013)

[11] S. SAARELMA, J. MARTIN-COLLAR ET AL., Plasma Phys. Control. Fusion, **59**, 064001 (2017)

[12] D. R. HATCH, D. TOLD ET AL., Nucl. Fusion, **55**, 063028 (2015)

[13] D. R. Hatch, M. Kotschenreuther et al., Nucl. Fusion, **56**, 104003 (2016)
[14] D. R. Hatch, M. Kotschenreuther et al., Nucl. Fusion, **57**, 036020 (2017)
[15] M. Kotschenreuther, D. R. Hatch et al., Nucl. Fusion, **57**, 064001 (2017)
[16] A. Diallo, J. W. Hughes et al., Phys Rev Lett, **112**, 115001 (2014)
[17] A. Diallo, R. J. Groebner et al., Phys. Plasmas, **22**, 056111 (2015)
[18] A. Diallo, J. W. Hughes et al., Nucl. Fusion, **55**, 053003 (2015)
[19] F. M. Laggner, E. Wolfrum et al., Plasma Phys. Control. Fusion, **58**, 065005 (2016)
[20] M. Cavedon, T. Pütterich et al., Plasma Phys. Control. Fusion, **59**, 105007 (2017)
[21] E. Wolfrum, E. Viezzer et al., Nucl. Fusion, **55**, 053017 (2015)
[22] R. L. Boivin, J. L. Luxon et al., Fusion Sci. Tech., **48**, 834 (2015)
[23] J. L. Luxon, Nucl. Fusion, **42**, 614 (2002)
[24] R. Neu, M. Balden et al., Plasma Phys. Control. Fusion, **49**, B59 (2007)
[25] R. Neu, A. Kallenbach et al., J. Nucl. Mater., **438**, S34 (2013)
[26] P. M. Anderson, C. B. Baxi et al., Fusion Eng. Des., **9**, 9 (1989)
[27] R. Fischer, C. J. Fuchs et al., Fusion Sci. Tech., **58**, 675 (2010)
[28] A. Mlynek, M. Reich et al., Nucl. Fusion, **51**, 043002 (2011)
[29] M. Willensdorfer, G. Birkenmeier et al., Plasma Phys. Control. Fusion, **56**, 025008 (2014)
[30] M. Willensdorfer, S. S. Denk et al., Plasma Phys. Control. Fusion, **58**, 114004 (2016)
[31] S. K. Rathgeber, L. Barrera et al., Plasma Phys. Control. Fusion, **55**, 025004 (2013)
[32] B. Kurzan, H. Murmann et al., Rev. Sci. Instrum., **72**, 1111 (2001)
[33] A. Kallenbach, A. Carlson et al., J. Nucl. Mater., **290**, 639 (2001)
[34] T. N. Carlstrom, G. L. Campbell et al., Rev. Sci. Instrum., **63**, 4901 (1992)
[35] D. Eldon, B. D. Bray et al., Rev Sci Instrum, **83**, 10E343 (2012)
[36] O. Meneghini, S. P. Smith et al., Nucl. Fusion, **55**, 083008 (2015)
[37] N. C. Logan, B. A. Grierson et al., Fusion Sci. Tech., **74**, 125 (2018)
[38] M. A. V. Zeeland and T. N. Carlstrom, Rev. Sci. Instrum., **75**, 3423 (2004)
[39] M. A. V. Zeeland, R. L. Boivin et al., Rev. Sci. Instrum., **77** (2006)
[40] R. J. Colchin, D. L. Hillis et al., Rev. Sci. Instrum., **74**, 2068 (2003)
[41] N. H. Brooks, R. J. Colchin et al., Rev Sci Instrum, **79**, 10F330 (2008)
[42] A. Burckhart, E. Wolfrum et al., Plasma Phys. Control. Fusion, **52**, 105010 (2010)
[43] R. J. Groebner, T. H. Osborne et al., Nucl. Fusion, **49**, 045013 (2009)
[44] R. J. Groebner, A. W. Leonard et al., Nucl. Fusion, **49**, 085037 (2009)
[45] R. J. Groebner, C. S. Chang et al., Nucl. Fusion, **53**, 093024 (2013)
[46] E. Viezzer, M. Cavedon et al., Nucl. Fusion, **58** (2018)
[47] Z. Yan, G. R. McKee et al., Phys. Plasmas, **18**, 056117 (2011)
[48] A. F. Mink, M. Hoelzl et al., Nucl. Fusion, **58** (2018)
[49] B. Vanovac, E. Wolfrum et al., Plasma Phys. Control. Fusion, **60** (2018)
[50] B. Vanovac, E. Wolfrum et al., accepted in Nucl. Fusion (2018)
[51] F. Mink, E. Wolfrum et al., Plasma Phys. Control. Fusion, **58**, 125013 (2016)
[52] F. M. Laggner, S. Keerl et al., Plasma Phys. Control. Fusion, **60** (2018)
[53] T. H. Osborne, J. R. Ferron et al., Plasma Phys. Control. Fusion, **42**, A175 (2000)
[54] M. G. Dunne, L. Frassinetti et al., Plasma Phys. Control. Fusion, **59**, 025010 (2017)
[55] F. M. Laggner, E. Wolfrum et al., Nucl. Fusion, **58** (2018)
[56] A. W. Degeling, Y. R. Martin et al., Plasma Phys. Control. Fusion, **45**, 1637 (2003)
[57] P. T. Lang, A. W. Degeling et al., Plasma Phys. Control. Fusion, **46**, L31 (2004)
[58] S. P. Gerhardt, J. W. Ahn et al., Nucl. Fusion, **50**, 064015 (2010)
[59] E. de la Luna, I. T. Chapman et al., Nucl. Fusion, **56**, 026001 (2016)
[60] F. J. Artola, G. Huijsmans et al., Nucl. Fusion (2018)
[61] P. T. Lang, A. Burckhart et al., Nucl. Fusion, **54**, 083009 (2014)
[62] A. Loarte, G. Huijsmans et al., Nucl. Fusion, **54** (2014)
[63] M. Knolker, A. Bortolon et al., Nucl. Fusion, **58** (2018)
[64] C. P. Perez, H. R. Koslowski et al., Plasma Phys. Control. Fusion, **46**, 61 (2004)
[65] X. Gao, T. Zhang et al., Plasma Sci. Technol., **15**, 732 (2013)
[66] H. Q. Wang, G. S. Xu et al., Nucl. Fusion, **54** (2014)
[67] W. L. Zhong, X. L. Zou et al., Plasma Phys. Control. Fusion, **58**, 065001 (2016)
[68] S. M. Kaye, J. L. Dunlap et al., Plasma Phys. Control. Fusion, **36**, A135 (1994)
[69] F. M. Laggner, E. Wolfrum et al., Phys. Plasmas, **24**, 056105 (2017)